https://doi.org/10.5194/egusphere-2025-2900
Preprint. Discussion started: 6 August 2025

Brief communication: Estimating Antarctic surface melt rates using passive microwave data calibrated with weather station observations.

Valeria Di Biase[1], Peter Kuipers Munneke[1], Bert Wouters[2], Michiel R. van den Broeke[1], and Maurice van Tiggelen[1]

[1]Institute for Marine and Atmospheric Research, Department of Physics, Utrecht University, Utrecht, the Netherlands
[2]Department of Geoscience & Remote Sensing, Delft University of Technology, Delft, the Netherlands

Correspondence: Valeria Di Biase (valedibiase@gmail.com)

Abstract.

We present a dataset of Antarctic annual surface melt rates (6.25 km resolution, 2012-2021) from 19 GHz Special Sensor Microwave Imager/Sounder (SSMIS). First, melt occurrence is detected via thresholds for brightness temperature, diurnal variation, and winter anomaly, calibrated with Automatic Weather Station (AWS) data. Second, AWS-driven surface energy balance modeling yields an empirical relation between annual melt days and water-equivalent melt volume. SSMIS-derived melt volumes show good agreement with AWS-based melt estimates ($R^2 = 0.83$). Compared to QuikSCAT and RACMO2.4 outputs, SSMIS captures a similar spatial melt pattern but estimates a total melt volume approximately 15% lower than RACMO, on the decadal average.

1 Introduction

The occurrence of surface melt on the Antarctic ice sheet constitutes a key indicator of cryospheric change, with profound implications for ice-shelf stability, glacier dynamics, and continental mass balance. Surface melting has been linked to ice-shelf thinning (Holland et al., 2011), accelerated outlet glacier flow, and sudden ice-shelf collapse (Scambos et al., 2000).

Remote sensing is a practical way to monitor surface melt across the vast Antarctic ice sheet. Passive-microwave radiometry exploits the strong contrast in brightness temperature between wet and dry snow (Zwally and Gloersen, 1977).The penetration depth of the microwave signal varies strongly with frequency — only a few centimetres at 37 GHz (∼2 cm), and increasing up to ∼1.8 m at 1.4 GHz — so that each channel samples a different layer of the snow/firn column (Colliander et al., 2022). Several studies have introduced binary melt-day detection approaches based on simple thresholds or polarization and spectral indices to identify liquid water (Zwally and Fiegles, 1994; Abdalati and Steffen, 1997; Torinesi et al., 2003; Picard and Fily, 2006). These approaches are indicators for the presence of liquid water, rather than for the actual physical process of surface melt, which is in fact an energy-conversion process (de Roda Husman et al., 2022). Yet, the term "surface melt" is widely used in the remote-sensing community (e.g., Torinesi et al. 2003, Trusel et al. 2013, Leduc-Leballeur et al. 2020, Banwell

https://doi.org/10.5194/egusphere-2025-2900
Preprint. Discussion started: 6 August 2025

et al. 2023), and we will adopt it here, although we acknowledge that passive-microwave sensors detect liquid water in the snowpack, independently of whether active melting is occurring at the surface.

From this point onward, we will refer to observations of liquid-water presence — whether derived from passive-microwave data or from in situ AWS measurements — collectively as "surface melt days."

These approaches provide valuable insights into the spatial and temporal distribution of melt days but do not directly yield water-equivalent melt volumes. A smaller but growing body of work has tackled the challenge of quantifying melt volumes from satellite data. Trusel et al. (2013) empirically calibrated active-microwave QuikSCAT Ku-band backscatter against automatic weather station (AWS) energy-balance estimates to produce continent-wide melt-volume maps at ∼4.5 km resolution. Unfortunately, the QuikSCAT mission ended in 2009. All efforts to quantify surface melt volume since then rely on model-based training data. For example, Zheng et al. (2022) used a neural network trained on modelled surface melt to estimate daily melt over Greenland from passive-microwave data at 3.125 km resolution. Banwell et al. (2023) combined passive-microwave and ASCAT scatterometer melt-day counts with the SNOWPACK firn model to derive meltwater volumes on ice shelves.

In this paper, we present the first method to estimate Antarctic melt-volume from passive microwave data that is calibrated solely against melt rate derived from in situ AWS surface energy balance (SEB) observations. We employ 19 GHz brightness temperatures from SSMIS on DMSP-F17, chosen for high sensitivity to small amounts of liquid water in the snowpack (de Roda Husman et al., 2022) and continuity with earlier SSM/I instruments which potentially enable long-term monitoring. Melt-day occurrence and the melt-day-to-volume relationship are both calibrated directly to melt volumes from seven AWS sites in Antarctica (Van Tiggelen et al., 2025; Jakobs et al., 2020). By using in situ observations for calibrating the satellite signal to melt volume, we incorporate directly critical physical feedbacks in the interaction between the snowpack and the atmosphere, such as temperature–albedo interactions (Jakobs et al., 2020), or refreezing dynamics. Through this multi-tiered approach — combining high-resolution SSMIS retrievals, AWS-SEB calibration, and model intercomparison — we deliver a reproducible, quantitative baseline for Antarctic surface melt and identify pathways for future methodological refinements.

2 Materials

This study relies on two main sources of data: satellite-derived brightness temperature from the SSMIS sensor and in-situ observations from AWS. These datasets are used for melt detection, calibration, and validation. The following subsections describe their characteristics and processing. We use the MEaSUREs Antarctic Boundaries Version 2 dataset (Mouginot, 2017) as the Antarctic mask. We define each Antarctic hydrological year as running from 1 June through 31 May of the following calendar year. In this study, we analyze ten hydrological years spanning 2012–2021 for availability of AWS data, corresponding to the period from 1 June 2011 to 31 May 2021.

2.1 SSMIS brightness temperature

This study uses SSMIS brightness temperature from the DMSP-F17 satellite over the period 2012–2021. DMSP-F17 was selected for its sun-synchronous, dawn–dusk orbit stability, which provides two consistent Antarctic overpasses per day at

https://doi.org/10.5194/egusphere-2025-2900
Preprint. Discussion started: 6 August 2025

approximately 06:00 (hereafter "M", morning observation) and 18:00 (hereafter "E", evening observation) local time[1]. All brightness temperatures were obtained from the National Snow and Ice Data Center (NSIDC)[2] and preprocessed in Google Earth Engine (Gorelick et al., 2017). Our analysis concentrates on the horizontally polarized 19 GHz channel, offering a 6.25 km × 6.25 km footprint — the finest available at this frequency. We also investigated the 37 and 91 GHz channels, as well as the vertically polarized signal, but found that it did not improve the melt detection method appreciably.

2.2 Automatic weather stations observations

Automatic weather station observations are the foundation for the method in this paper. For the melt volume to be calculated, only AWS that measure sufficient variables to close the surface energy balance qualify. This grossly reduces the number of available AWS locations, since the full radiation budget is only measured at a handful of stations in Antarctica. A major provider of data for this study is the Institute for Marine and Atmospheric Research Utrecht (IMAU) AWS dataset, which is described in Van Tiggelen et al. (2025). Only the IMAU AWS stations with at least one entire hydrological year of data within the June 2011 – May 2021 window were used for calibration and evaluation. These comprise AWS11 (Halvfarryggen Ice Rise), AWS14 (northern Larsen C ice shelf), AWS15 (central Larsen C ice shelf), AWS16 (Princess Elisabeth station), AWS17 (Scar Inlet as a remnant of Larsen B ice shelf) and AWS18 (Cabinet Inlet on western Larsen C ice shelf). All six sites record the standard meteorological variables and the four components of net surface radiation, with measurements corrected for common errors as detailed in Van Tiggelen et al. (2025). Melt volumes are subsequently computed at each station using the SEB model of Jakobs et al. (2020). In this framework, turbulent fluxes are calculated using similar theory, surface temperature is determined via iterative closure of the SEB, and excess energy at 0°C is converted into meltwater. Meltwater percolates through the firn using a bucket scheme until refreezing occurs. Shortwave radiation penetration into the snowpack is neglected. Of the six IMAU AWS stations meeting our requirements, four (AWS14, AWS15, AWS17 and AWS18) are situated on or immediately adjacent to Larsen C ice shelf, whereas the remaining two (AWS11 and AWS16) provide a few years of measurements in locations with low melt. To broaden the geographic scope of our calibration and ensure robust performance of the melt model across climatically distinct regions, we augment the IMAU network with a decade (2012–2021) of observations at the German Neumayer station, where we use the surface radiation observations from the Baseline Surface Radiation Network (BSRN) station (Schmithüsen, 2021), meteorological observations (Schmithüsen, 2023a), and surface height observations (Schmithüsen, 2023b).

For additional analysis, we also use observations of near-surface air temperature scaled to a nominal height of 2 m above the surface.

Modelling surface melt in an SEB model carries uncertainties because of model settings, model assumptions, and errors in the input. This uncertainty is estimated using a number of sensitivity tests. First, the uncertainty from the IMAU AWS forcing is estimated by separately including or removing one of four measurement corrections: the window heating of the pyrgeometer, the shortwave heating of the passively ventilated temperature sensor, the correction for relative humidity for ice and sensor sen-

[1] https://www.remss.com/missions/ssmi/
[2] https://nsidc.org/data/nsidc-0630/versions/2, last accessed 6 June 2025

https://doi.org/10.5194/egusphere-2025-2900
Preprint. Discussion started: 6 August 2025

sitivity at very low temperatures, and the correction for tilt and bias of the pyranometer, which are all described by Van Tiggelen et al. (2025). Then, the uncertainty due to the SEB model settings and assumptions is estimated by separately varying one of five model settings at the time: using a constant height of the sensors to 2 m above the surface instead of variable in time, the use of a roughness length for momentum of 1 mm instead of 0.1 mm for snow, using a surface longwave emissivity of 0.97 instead of 1, using an alternative snow thermal conductivity (Anderson, 1976), and finally, letting the snow height freely evolve in the model instead of prescribing snow height in time using the sonic height ranger observations. These choices result in one reference and nine perturbed time series of SEB components and surface melt per IMAU station, where each perturbed timeseries results from just one omitted measurement correction or one different model parameter at the time. This sensitivity analysis was conducted only for the AWS stations with the highest number of positive melt observations among those selected, namely AWS14, AWS15, AWS17, and AWS18.

3 Methods

We derive the occurrence of a surface melt day and annual melt totals over Antarctica in two steps. First, we calibrate SSMIS brightness temperature against in-situ surface melt observations at AWS locations to identify robust thresholds that discriminate surface melt from non-melt days (Sec. 3.2). Second, we translate SSMIS-derived melt-day counts to a water-equivalent surface melt volume using an empirical relation derived from the AWS observations (Sec. 3.3).

Prior to these steps, we have to establish that satellite observations at a spatially averaged scale of 6.25 km x 6.25 km are representative of AWS observations at a singular point.

3.1 Melt homogeneity

To assess whether the selected 6.25 km $\times$ 6.25 km SSMIS pixel accurately represents melt conditions at each AWS site, we compared it against the higher-resolution U-Melt binary melt product (de Roda Husman et al., 2024), available at 500 m spatial resolution. For each station, an 11 $\times$ 11 pixel window centered on the AWS location was extracted, and the 0/1 melt flags of all surrounding pixels were compared to that of the central pixel.

Two metrics were computed: (i) *Homogeneity rate*, defined as the fraction of surrounding pixels with melt flags matching the central pixel, which exceeded 99% at all stations; and (ii) *Local variability*, defined as the standard deviation of binary melt values within the window, consistently below 0.01.

These results indicate that, despite the $\sim$40 km^2 native footprint of a SSMIS pixel, melt conditions around each AWS site are highly homogeneous. Therefore, the selected SSMIS pixel provides a reliable representation of local melt conditions and is appropriate for calibration purposes.

3.2 SSMIS Melt Detection: Calibration and Flagging

To translate SSMIS brightness temperatures (T_b) into surface melt-day detections, we assembled a suite of candidate indicators drawn from established microwave-based methods and calibrated each against in situ AWS melt observations ($\geq$ 0.5

https://doi.org/10.5194/egusphere-2025-2900
Preprint. Discussion started: 6 August 2025

mm w.e. day^{-1}). All metrics were computed at 19 GHz, 37 GHz, and 91 GHz, using both horizontal (H) and vertical (V) polarizations. The indicators were grouped as follows (see Table S1 for a detailed description of all candidate variables):

1. *Pure Brightness-Temperature:* We tested absolute T_b at each frequency and polarization, for both morning and evening observations.

2. *Winter-Anomaly:* Difference between the T_b and its winter mean (Zwally and Gloersen, 1977).

3. *Diurnal and Day-to-Day Change:* i) Diurnal amplitude: difference in T_b between evening and morning overpasses (Ramage and Isacks, 2002). ii) Day-to-day change: difference in T_b between consecutive days at the same overpass time.

4. *Normalized Polarimetric Ratio (NPR):* Contrast between vertical and horizontal polarizations at the same frequency and overpass (Abdalati and Steffen, 1997).

5. *Normalized Seasonal Anomalies:* Indicators that account for seasonal variability by comparing T_b to its winter anomaly plus a multiple of the winter or annual standard deviation (Torinesi et al., 2003).

Each candidate indicator's day-by-day values were compared against AWS-derived melt versus non-melt classifications. Receiver Operating Characteristic (ROC) analysis was performed on all candidates (Fig. S1), and thresholds were chosen to achieve an optimal trade-off between true positive rate (TPR) and false positive rate (FPR). The two best-performing metrics were the 19 GHz H polarization evening brightness temperature, $T_{b,19\mathrm{H}}^{(E)}$ (TPR $\approx 62\%$, FPR $\approx 2\%$), and its diurnal amplitude (TPR $\approx 67\%$, FPR $\approx 3\%$). All other candidates yielded TPR below 50%.

3.2.1 Multivariate Optimization

Since no single indicator achieved both high TPR and true negative rate (TNR; i.e., 1 - FPR) we selected triplets from the analyzed metrics and applied logical rules i) *and* (all three thresholds must be exceeded for a melt day to be detected); ii) *or* (at least one threshold must be exceeded); iii) *majority* (at least two thresholds must be exceeded) to their thresholds. In 1,000 Monte Carlo trials (randomly sampling 30% of melt and 30% of non-melt days), the *majority* rule achieved the highest overall accuracy and the resulting thresholds exhibited near-Gaussian distributions (Fig. S2). The optimal threshold combination under the majority rule is:

$$\{T_{b,19\mathrm{H}}^{(E)} > 219.2\,\mathrm{K},\ \Delta T_d > 19.7\,\mathrm{K},\ A_w > 26.3\,\mathrm{K}\},$$

where

$$\Delta T_d = T_{b,19\mathrm{H}}^{(E)} - T_{b,19\mathrm{H}}^{(M)},$$

denotes the diurnal amplitude (difference between evening (E) and morning (M) overpasses), and

$$A_w = T_{b,19\mathrm{H}}^{(E)} - \mu_{\mathrm{winter}},$$

https://doi.org/10.5194/egusphere-2025-2900
Preprint. Discussion started: 6 August 2025

is the winter anomaly, with μ_{winter} representing the mean 19 GHz horizontal-polarization brightness temperature over 1 June–31 August.

This triplet yields 95.3% accuracy (TPR = 77.8%, TNR = 97.2%), thus balancing false positives and false negatives. Importantly, because negative samples greatly outnumber positive ones in our dataset, a 3% drop in TNR (i.e., more false positives) produces an absolute error count roughly equivalent to that resulting from a 22% drop in TPR (i.e., more false negatives). This analysis is conducted on an annual basis, and the balanced trade-off between false positives and false negatives is achieved at this temporal scale; applying the same thresholds over shorter periods may lead to a disproportionate increase in one error type. At annual temporal resolution, a 3% decrease in TNR produces an absolute error count comparable to that from a 22% decrease in TPR, demonstrating a balanced trade-off between the two error types at this scale.

3.2.2 Melt-Day Flagging and Annual Summation

These three criteria were applied to each set of two daily SSMIS overpasses for each pixel. A pixel is flagged as "melt" on day d if at least two thresholds are met. Annual melt-day counts are obtained by summing these daily flags per pixel over an Antarctic year (1 Jun to 31 May). A linear regression between AWS-derived and SSMIS-derived annual melt-day counts yielded a coefficient of determination of $R^2 = 0.91$ (Fig. 1a).

3.3 Melt estimation

The second major step in the melt volume estimate is to relate the annual number of melt days (m) to total annual melt (M). To that end, we fitted the AWS-derived decadal record (2012-2021) to an exponential model:

$$M = a\left(e^{b\,m} - 1\right), \tag{1}$$

where parameters a and b were estimated using a least-squares approach to minimize the residuals between the model and the observed melt values (Fig. 2a). The above functional form follows an empirically demonstrated non-linear relationship between melt days and meltwater production (Banwell et al., 2023; Trusel et al., 2013). This non-linear behaviour likely reflects melt-albedo feedbacks, and the longer time required for refreezing of larger melt volumes, such that warmer summers produce disproportionately more runoff (Banwell et al., 2023). By fitting a and b from equation 1 to AWS stations, which compute melt via a full SEB model, our approach embeds these physical feedbacks into the satellite-only framework.

When the exponential model is applied to the satellite-derived melt-day count, a pixel-level estimate of annual melt is obtained. A Monte Carlo-based confidence interval for the m–M relationship is derived by propagating measurement and model uncertainties (detailed in Sec. 2.2, see Fig. 2a): for each AWS-year combination, ten m–M pairs corresponding to distinct setups are available, and in each of 1000 Monte Carlo iterations one setup is randomly selected for each AWS-year, yielding n data points. The exponential model of 1 is then fitted to each sample, producing 1000 realizations of $M(m)$ which are evaluated over $m \in [0, 100]$ to characterize the variability of melt estimates. The light pink band in Fig. 2a represents the 3σ confidence envelope, the blue line denotes the median-fit relationship, and the red line corresponds to the fit obtained using the reference

https://doi.org/10.5194/egusphere-2025-2900
Preprint. Discussion started: 6 August 2025

setup alone.

Fig. S3a shows the site-specific exponential fits at each of the four AWS locations (AWS14, AWS15, AWS17, AWS18) where the sensitivity analysis was conducted (see Sec. 2.2); Fig. S3b presents the combined fit across the selected four AWS stations, illustrating how the ten SEB-model permutations produce a modest spread in the resulting m–M curves.

For an independent assessment of the m–M relation, it was also derived for fully independent, model-only, RACMO2.4 melt-day and melt-volume output for 2012–2021, both across the entire Antarctic domain (Fig. 2b) and separately at four selected AWS locations (see Fig. S3c). In both cases, the resulting exponential parameters and curve shape closely matched those derived from the AWS-SEB calibration, demonstrating the robustness and spatial generality of the m–M relationship. This also demonstrates that the collection of AWS observations used for this study sufficiently captures the variability in surface melt conditions across the Antarctic ice sheet as represented by a physically-based model. The agreement in functional shape, despite the melt days underestimation by SSMIS, supports the application of the AWS-derived fit to satellite-derived melt-day counts across the full Antarctic dataset.

4 Results

4.1 SSMIS-AWS comparison

Applying the fit described in Section 3.3, we produced estimates of total annual melt across Antarctica (Fig. 3a). We assessed our results by comparing annual SSMIS-derived melt days and melt fluxes with coincident AWS-based observations, yielding a strong linear correlation ($R^2 = 0.91$ and $R^2 = 0.83$, respectively; Fig. 1b). However, given the limited number of in situ AWS sites — which were also employed during calibration — this evaluation is inherently circular. Dividing the AWS record into independent calibration and validation subsets was considered not feasible due to the small sample size and the constrained spatial variability of the available stations.

4.2 Comparison of SSMIS with QuikSCAT and RACMO2.4p1

We compare our ten-year mean melt-flux estimates from SSMIS with two independent products:

- **QuikSCAT (1999–2009)**: active-microwave backscatter retrieval of annual melt flux at 4.45 km resolution (Trusel et al., 2013), see Fig. 3b.
- **RACMO2.4 (2012–2021)**: regional climate model forced by ERA5, providing daily melt flux at 11 km resolution, here averaged to the same decadal period (van Dalum et al., 2025), see Fig. 3c.

Broad spatiotemporal agreement exists among all three products. On Larsen C ice shelf, SSMIS, QuikSCAT, and RACMO melt rates exceed 350 mm w.e. yr^{-1}. However, SSMIS and QuikSCAT (1999–2009) show their highest values on the western inlets (e.g. Mill Inlet), whereas RACMO's peak is shifted eastward toward Scar Inlet, a discrepancy noted earlier (Trusel et al., 2013).

https://doi.org/10.5194/egusphere-2025-2900
Preprint. Discussion started: 6 August 2025

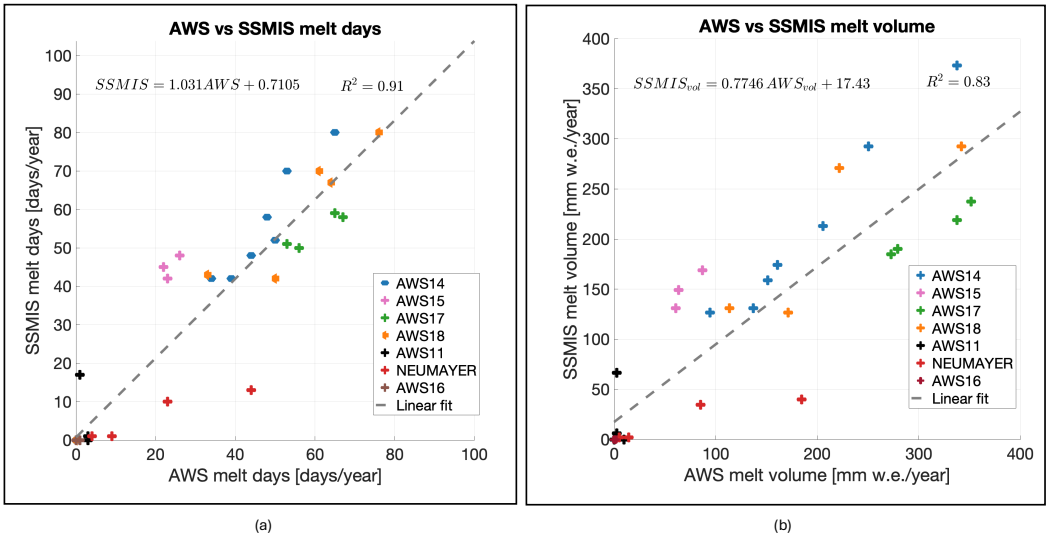

Figure 1. Evaluation of all available coincident SSMIS- and AWS-based (a) melt days and (b) melt fluxes across the seven AWS locations.

Western-Peninsula ice shelves such as Wilkins and George VI exhibit mean melt fluxes higher than 200–250 mm w.e. yr^{-1} in all three datasets. On Shackleton Ice Shelf, all products report peak fluxes around 200-250 mm w.e. yr^{-1} along the outer coastal margin.

In Dronning Maud Land, annual surface melt at Roi Baudouin and inner Fimbul ice shelves are consistently around 200 mm w.e. yr^{-1}, while northeast Amery Ice Shelf peaks around 150 mm w.e. yr^{-1} across SSMIS, QuikSCAT, and RACMO. Along the Ross and Amundsen Sea margins, each method records low-intensity melting (20–30 mm w.e.,yr^{-1}). Over the Ross Ice Shelf, SSMIS and QuikSCAT indicate that melt occurs predominantly on the western side, whereas RACMO simulates the strongest melt on the eastern margin. Finally, to facilitate a direct comparison with QuikSCAT, RACMO2.4p1 outputs were extracted for 1999–2009 (Fig. 3d). During this interval, both datasets exhibit comparable magnitudes (mean values within $\sim$10%) and analogous large-scale spatial distributions, despite RACMO's modest eastward shift in melt maxima and QuikSCAT's systematic underestimation of low-melt zones. These inter-product agreements and discrepancies parallel those observed between SSMIS and RACMO for 2012–2021.

Interannual melt volumes from SSMIS and RACMO over 2012–2021 exhibit very similar temporal patterns, with mean annual melt fluxes over 2012–2021 of approximately 83 Gt yr^{-1} for SSMIS compared to 98 Gt yr^{-1} for RACMO (Fig. S4). The corresponding yearly mean surface melt flux maps (SSMIS vs. RACMO), presented in Fig. S5 of the Supplementary Materials, further highlight the strong agreement in both spatial and temporal variability between the two datasets.

https://doi.org/10.5194/egusphere-2025-2900
Preprint. Discussion started: 6 August 2025

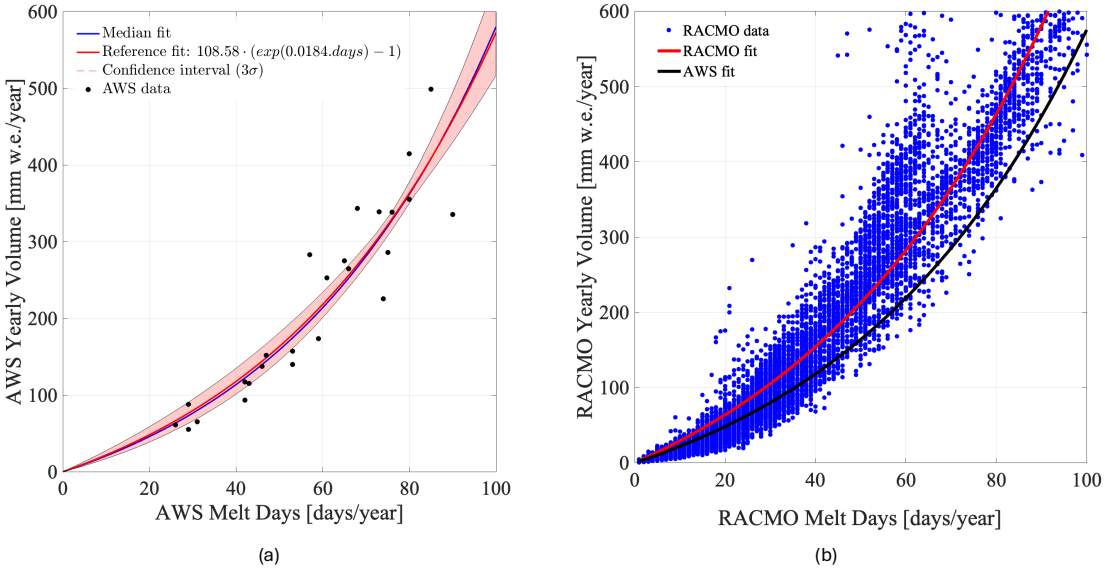

Figure 2. Exponential melt-day to melt-volume relationship. **(a)** Scatterplot of annual meltwater volume (M, from AWS-SEB) versus melt days (m) at six IMAU-AWS stations for 2012–2021, with the best-fit exponential curve shown in red. The median fit from 1,000 Monte Carlo realizations is shown in blue, and the shaded pink band indicates the $\pm 3\sigma$ confidence interval. **(b)** Comparison of the AWS-derived m–M curve (black) against RACMO2.4p1: the red line is the RACMO fit, while blue dots represent RACMO2.4p1 pixel-level data for all of Antarctica over 2012–2021.

5 Discussion

A closer look at misclassified days reveals two primary sources of false positive detections. About 71 % of false positives occur when RACMO2.4p1 simulates non-zero liquid water content (LWC) in the firn (See Fig. S6a). Nearly 90 % of false positives coincide with AWS near-surface air temperatures (T_{2m}) above –5 °C (See Fig. S6b). These findings suggest that our classifier is not only responding to surface melt events, but more generally detects the presence of liquid water near the surface (de Roda Husman et al., 2022), e.g., water retention within the upper firn that elevates brightness temperature above the winter offset. In this sense, SSMIS appears sensitive to a broader melt signal spectrum, including processes not directly measurable by AWS but captured by RACMO's subsurface hydrology. For this reason, we also explored the potential of additional microwave indicators, such as the 37 GHz channel and various polarization or spectral ratios, to reduce false positives by improving sensitivity to surface wetting. While these metrics offer theoretical advantages due to their shallower penetration and enhanced surface melt response (Colliander et al., 2022), our cross-validation results show no consistent performance improvement across the AWS network. This outcome supportes the assumption that the 19 GHz H polarization signal remains

https://doi.org/10.5194/egusphere-2025-2900
Preprint. Discussion started: 6 August 2025

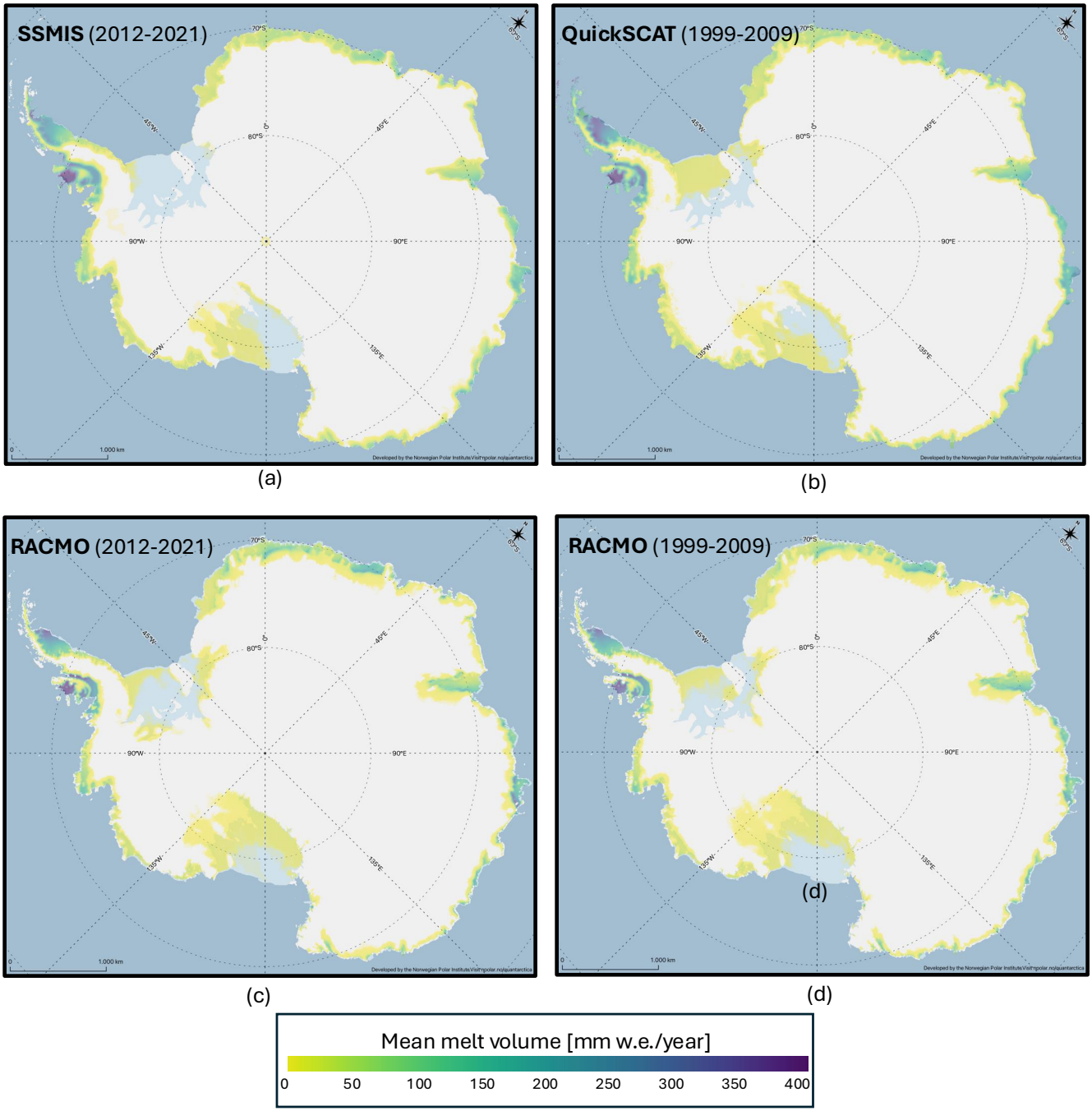

Figure 3. Comparison of decadal mean meltwater volume across Antarctica. (a) SSMIS-derived annual melt flux averaged over 2012–2021. (b) QuikSCAT-derived melt flux over 1999–2009 from backscatter observations (Trusel et al., 2013). (c) RACMO2.4p1 model output averaged over 2012–2021 (van Dalum et al., 2025). (d) RACMO2.4p1 model output averaged over 1999–2009 (van Dalum et al., 2025).

https://doi.org/10.5194/egusphere-2025-2900
Preprint. Discussion started: 6 August 2025

the most stable and spatially representative choice under current sensor constraints. A closer examination of Fig. 1 shows that Neumayer station exhibits larger residuals than the other sites. This discrepancy likely reflects Neumayer's local climate, where subfreezing daytime temperatures drive nearly instantaneous firn refreezing (van den Broeke et al., 2010). Consequently, less liquid water remains at the surface during SSMIS overpasses, diminishing the brightness-temperature signal compared to other AWS locations — such as Larsen C — where subsurface water retention prolongs wet-snow signatures.

From a spatial perspective, our melt product reveals interesting regional features. For instance, on the Larsen C ice shelf, a distinct east-west gradient is visible, likely driven by föhn winds over the Antarctic Peninsula mountain range (Luckman et al., 2014) and supported by melt patterns in QuikSCAT (Trusel et al., 2013), and firn air content observations across the ice shelf (Holland et al., 2011). The SSMIS-based method underestimates surface melt relative to QuikSCAT — but the first was collected a decade prior to the second. Thus, its difference may be attributed to the documented cooling trend over the Peninsula after 2000 (Turner et al., 2016). Taken together, our findings suggest that the proposed SSMIS-based detection scheme reasonably captures the spatial and temporal patterns of surface melt across Antarctica. Its general consistency with known climate trends indicates that the classifier is likely robust to both environmental variability and regional melt characteristics. However, the sensitivity to shallow wetting layers — while offering valuable insight into subsurface processes — also introduces uncertainty when interpreting daily melt flags. Refining this ambiguity represents a necessary direction for improving the distinction between surface and subsurface melt in future satellite-based algorithms.

6 Conclusions

We introduce a novel 6.25 km gridded dataset of Antarctic surface melt rates for 2012–2021, derived exclusively from SSMIS 19 GHz passive-microwave observations and calibrated against seven AWS energy-balance melt records. Our majority-rule framework—combining absolute evening T_b, diurnal amplitude, and winter-season anomaly—yields daily melt flags that, when transformed through an exponential melt-day to melt-volume model, reproduce in-situ melt volumes with fidelity. Comparative analyses with QuikSCAT and RACMO2.4p1 confirm that our product accurately maps melt hotspots, while misclassification analysis clarify the conditions under which passive-microwave retrievals are least reliable.

By providing a spatially comprehensive, satellite-only record of Antarctic surface melt, this dataset fills a critical gap between sparse in-situ measurements and model outputs. It offers a transparent, reproducible baseline for evaluating regional climate models, constraining firn-hydrology schemes, and informing assessments of ice-shelf vulnerability to meltwater-induced weakening. The complete Antarctic-wide, decadal melt record is publicly available for use in cryospheric process studies.

Code and data availability. The annual Antarctic surface melt–water equivalent maps derived from SSMIS 19 GHz brightness temperatures, covering the period 2011–12 to 2020–21, are publicly available at https://doi.org/10.5281/zenodo.16738423 (Di Biase, 2025). The dataset includes GeoTIFF files providing annual number of melt days and cumulative annual melt volume per pixel (in mm water equivalent) with corresponding lower/upper bound estimates based on the confidence intervals represented in Fig.2(a) to convey the uncertainty range.

https://doi.org/10.5194/egusphere-2025-2900
Preprint. Discussion started: 6 August 2025

The AWS data used as forcing for the SEB model is available at https://doi.pangaea.de/10.1594/PANGAEA.974080 (Van Tiggelen et al., 2024). The SEB model used to compute surface melt is available at https://doi.org/10.5281/zenodo.15082295 (Van Tiggelen et al., 2025).

Author contributions. VDB developed the methodology, carried out validation, performed the formal analysis and investigation, curated the SSMIS data, and wrote the original draft. MvT contributed to the study conceptualization, managed AWS data curation, review and editing of the manuscript. PKM, BW, and MvdB contributed significantly to the overarching conceptual framework, supervised the research, the review and editing of the final manuscript.

Competing interests. B.W. and M.vdB. are members of the editorial board of journal The Cryosphere.

Acknowledgements. The authors would like to thank Christiaan van Dalum for providing the RACMO2.4p1 dataset, which was instrumental in the comparative analyses presented in this study.

The authors would also like to thank the members of the Institut des Géosciences de l'Environnement (IGE, Grenoble Alpes, France) for the valuable suggestions and fruitful exchanges throughout the development of this work.

https://doi.org/10.5194/egusphere-2025-2900
Preprint. Discussion started: 6 August 2025

References

Abdalati, W. and Steffen, K.: Snowmelt on the Greenland ice sheet as derived from passive microwave satellite data, Journal of Climate, 10, 165–175, 1997.

Anderson, E.: A point energy and mass balance model of a snow cover, Techn. Rep. NWS19, NOAA, 1976.

Banwell, A. F., Wever, N., Dunmire, D., and Picard, G.: Quantifying Antarctic-wide ice-shelf surface melt volume using microwave and firn model data: 1980 to 2021, Geophysical Research Letters, 50, e2023GL102 744, 2023.

Colliander, A., Mousavi, M., Marshall, S., Samimi, S., Kimball, J. S., Miller, J. Z., Johnson, J., and Burgin, M.: Ice sheet surface and subsurface melt water discrimination using multi-frequency microwave radiometry, Geophysical Research Letters, 49, e2021GL096 599, 2022.

de Roda Husman, S., Hu, Z., Wouters, B., Munneke, P. K., Veldhuijsen, S., and Lhermitte, S.: Remote Sensing of Surface Melt on Antarctica: Opportunities and Challenges, IEEE Journal of Selected Topics in Applied Earth Observations and Remote Sensing, https://doi.org/10.1109/JSTARS.2022.3216953, 2022.

de Roda Husman, S., Lhermitte, S., Bolibar, J., Izeboud, M., Hu, Z., Shukla, S., van der Meer, M., Long, D., and Wouters, B.: A high-resolution record of surface melt on Antarctic ice shelves using multi-source remote sensing data and deep learning, Remote Sensing of Environment, 301, 113 950, 2024.

Di Biase, V.: Annual Antarctic Surface Melt Maps (2011–12 to 2020–21) from SSMIS 19 GHz, Zenodo [Data set], https://doi.org/10.5281/zenodo.16738423, 2025.

Gorelick, N., Hancher, M., Dixon, M., Ilyushchenko, S., Thau, D., and Moore, R.: Google Earth Engine: Planetary-scale geospatial analysis for everyone, Remote sensing of Environment, 202, 18–27, 2017.

Holland, P. R., Corr, H. F., Pritchard, H. D., Vaughan, D. G., Arthern, R. J., Jenkins, A., and Tedesco, M.: The air content of Larsen ice shelf, Geophysical Research Letters, 38, 2011.

Jakobs, C. L., Reijmer, C. H., Smeets, C. J., Trusel, L. D., Van De Berg, W. J., Van Den Broeke, M. R., and Van Wessem, J. M.: A benchmark dataset of in situ Antarctic surface melt rates and energy balance, Journal of Glaciology, 66, 291–302, https://doi.org/10.1017/jog.2020.6, 2020.

Leduc-Leballeur, M., Picard, G., Macelloni, G., Mialon, A., and Kerr, Y. H.: Melt in Antarctica derived from Soil Moisture and Ocean Salinity (SMOS) observations at L band, The Cryosphere, 14, 539–548, 2020.

Luckman, A., Elvidge, A., Jansen, D., Kulessa, B., Munneke, P. K., King, J., and Barrand, N. E.: Surface melt and ponding on Larsen C Ice Shelf and the impact of föhn winds, Antarctic Science, 26, 625–635, 2014.

Mouginot, J.: MEaSUREs Antarctic boundaries for IPY 2007-2009 from satellite radar, Version 2, (No Title), 2017.

Picard, G. and Fily, M.: Surface melting observations in Antarctica by microwave radiometers: Correcting 26-year time series from changes in acquisition hours, Remote sensing of environment, 104, 325–336, 2006.

Ramage, J. M. and Isacks, B. L.: Determination of melt-onset and refreeze timing on southeast Alaskan icefields using SSM/I diurnal amplitude variations, Annals of Glaciology, 34, 391–398, 2002.

Scambos, T. A., Hulbe, C., Fahnestock, M., and Bohlander, J.: The link between climate warming and break-up of ice shelves in the Antarctic Peninsula, Journal of Glaciology, 46, 516–530, 2000.

Schmithüsen, H.: Basic and other measurements of radiation at Neumayer Station (1992-04 et seq), https://doi.org/10.1594/PANGAEA.932418, 2021.

https://doi.org/10.5194/egusphere-2025-2900
Preprint. Discussion started: 6 August 2025

Schmithüsen, H.: Continuous meteorological observations at Neumayer station (1982-03 et seq), https://doi.org/10.1594/PANGAEA.962313, 2023a.

Schmithüsen, H.: High resolved snow height measurements at Neumayer Station, Antarctica (2010 et seq), https://doi.org/10.1594/PANGAEA.958970, 2023b.

Torinesi, O., Fily, M., and Genthon, C.: Variability and trends of the summer melt period of Antarctic ice margins since 1980 from microwave sensors, Journal of Climate, 16, 1047–1060, 2003.

Trusel, L. D., Frey, K. E., Das, S. B., Munneke, P. K., and Van Den Broeke, M. R.: Satellite-based estimates of Antarctic surface meltwater fluxes, Geophysical Research Letters, 40, 6148–6153, 2013.

Turner, J., Lu, H., White, I., King, J. C., Phillips, T., Hosking, J. S., Bracegirdle, T. J., Marshall, G. J., Mulvaney, R., and Deb, P.: Absence of 21st century warming on Antarctic Peninsula consistent with natural variability, Nature, 535, 411–415, 2016.

van Dalum, C. T., van de Berg, W. J., van den Broeke, M. R., and van Tiggelen, M.: The surface mass balance and near-surface climate of the Antarctic ice sheet in RACMO2. 4p1, EGUsphere, 2025, 1–40, 2025.

van den Broeke, M., Bus, C., Ettema, J., and Smeets, P.: Temperature thresholds for degree-day modelling of Greenland ice sheet melt rates, Geophysical Research Letters, 37, 2010.

Van Tiggelen, M., Smeets, P. C. J. P., Reijmer, C. H., Kuipers Munneke, P., van den Broeke, M. R., Oerter, H., Eisen, O., Steinhage, D., Kipfstuhl, S., van Lipzig, N. P. M., Mangold, A., Lhermitte, S., and Lenaerts, J. T. M.: IMAU Antarctic automatic weather station data, including surface radiation balance (1995-2022), https://doi.org/0.1594/PANGAEA.974080, 2024.

Van Tiggelen, M., Smeets, P. C. J. P., Reijmer, C. H., Kuipers Munneke, P., and van den Broeke, M. R.: IMAU-ice-and-climate/IMAU-pyEBM, https://doi.org/10.5281/zenodo.15082294, 2025.

Van Tiggelen, M., Smeets, P. C. J. P., Reijmer, C. H., Kuipers Munneke, P., and van den Broeke, M. R.: IMAU Antarctic automatic weather station data, including surface radiation balance (1995–2022), Earth System Science Data Discussions, pp. 1–38, https://doi.org/10.5194/essd-2025-88, 2025.

Zheng, L., Cheng, X., Shang, X., Chen, Z., Liang, Q., and Wang, K.: Greenland Ice Sheet daily surface melt flux observed from space, Geophysical Research Letters, 49, e2021GL096 690, 2022.

Zwally, H. J. and Fiegles, S.: Extent and duration of Antarctic surface melting, Journal of Glaciology, 40, 463–475, 1994.

Zwally, H. J. and Gloersen, P.: Passive microwave images of the polar regions and research applications, Polar Record, 18, 431–450, 1977.